Acta Biomaterialia 9 (2013) 5360–5368

Contents lists available at SciVerse ScienceDirect

Acta Biomaterialia

journal homepage: www.elsevier.com/locate/actabiomat

In situ doxorubicin–CaP shell formation on amphiphilic gelatin–iron oxide core as a multifunctional drug delivery system with improved cytocompatibility, pH-responsive drug release and MR imaging

W.-M. Li, S.-Y. Chen *, D.-M. Liu *

Department of Materials Sciences and Engineering, National Chiao Tung University, Hsinchu 30010, Taiwan

ARTICLE INFO

Article history:
Received 6 June 2012
Received in revised form 11 September 2012
Accepted 19 September 2012
Available online 26 September 2012

Keywords:
Calcium phosphate
pH-sensitivity
Drug release
Amphiphilic gelatin
MR imaging

ABSTRACT

An amphiphilic gelatin–iron oxide core/calcium phosphate shell (AGIO@CaP-DOX) nanoparticle was successfully synthesized as an efficient anti-cancer drug delivery system, where doxorubicin (DOX) as a model molecule was encapsulated by electrolytic co-deposition during CaP shell formation. The shell of CaP precipitate played a pivotal role, not only in acting as a drug depot, but also in rendering the drug release rate in a highly pH-dependent controlled manner. Together with MR imaging, highly biocompatible drug-carrying CaP shell and efficient cellular internalization, the AGIO@CaP-DOX nanoparticles developed in this study area promising multifunctional nanodevice for nanotherapeutic approaches.

1. Introduction

Advanced delivery systems for anticancer drugs often use environmental stimuli to trigger a desired dose for therapeutic medication, while enhancing medical efficacy with fewer side effects. For example, the extracellular pH in tumor tissue is lower than that in normal tissue, and the pH-responsive carriers would accelerate drug release in tumor tissue [1]. In addition, the acidic cellular environment, such as in endosome and lysosome, also increases the efficacy of anticancer drugs via pH-initiated release of drugs [2]. The common delivery nanocarriers, such as liposomes [3], nanohydrogels, mesoporous silica nanoparticles and micelles [4], can easily solubilize and encapsulate poorly water-soluble drugs into their core structure. However, these candidates are also physico-chemically unstable and, consequently, subject to unexpected drug leakage. Therefore, it is essential to prevent or minimize natural leakage upon practical medication and, in the meantime, to improve efficiency in the delivery of drug carriers via surface modification, such as forming a thin shell on the surface of drug-carrying nanoparticles [5,6]. Numerous studies in the literature over the past decades have employed organic substances to modify the surface of carriers with improved biofunctionalities [7], including biocompatibility [8], stimuli-triggered release [9] and molecular recognition (targeting capability). However, reports addressing the use of inorganic substances such as silica [10,11], titania [12] and calcium phosphates [13,14] in the development of nanoparticulate drug delivery systems are comparatively less extensive.

Calcium phosphate (CaP) precipitates have long been well recognized as highly biocompatible and bioactive substances, based on their homology with natural inorganic materials such as teeth and bones. CaP has received much attention in the biomedical community, with several advantages over existing organic and inorganic counterparts [15]. First, CaP is able to bind and encapsulate drug or nucleic acids [16,17], and its extraordinary bioactivity and biocompatibility enables protection of the encapsulated molecules from enzymatic degradation, while efficiently delivering into cells [18]. Second, the delivery activity is probably related to the fact that CaP rapidly dissolves in the acidic environment and remains stable in a natural environment. Third, CaP is expected to be dissociated in endosomes/lysosome to induce endosomal/lysosomal membrane disruption with high osmotic pressure, and release its cargo into the cytoplasm [19]. Recently, the use of CaP as a surface modifier to form a shell structure on a drug-containing core phase for drug delivery with improved cytocompatibility has received considerable attention [20,21]. However, advanced drug delivery systems with multifunctionality have been an emerging trend in the development of modern biomedical technology, especially in nanomedicinal applications. The combining merits of improved cytocompatibility, strong MR imaging contrast, and highly environmental response from a controlled assembly of individual components ensure a promising drug delivery vehicle for

* Corresponding authors. Tel.: +886 3 5712121x31818 (S.-Y. Chen), +886 3 5712121x55391 (D.-M. Liu).
E-mail addresses: sanyuanchen@mail.nctu.edu.tw (S.-Y. Chen), deanmo_liu@yahoo.ca (D.-M. Liu).

1742-7061/$ - see front matter © 2012 Acta Materialia Inc. Published by Elsevier Ltd. All rights reserved.
http://dx.doi.org/10.1016/j.actbio.2012.09.023

advanced therapeutic purposes. In this work, a core–shell nanoparticle using a self-assembled amphiphilic gelatin was developed in the present authors' laboratory to direct the aggregation of iron oxide nanocrystallites [22] and form amphiphilic gelatin–iron oxide (AGIO) nanoparticles. Following rapid precipitation of CaP mineral with a controlled Ca/P ratio, a thin layer along the surface of AGIO can be constructed. To further facilitate drug loading during CaP shell formation, an anticancer drug doxorubicin (DOX) was employed as a model molecule to explore the feasibility of simultaneous co-deposition of the DOX–CaP layer on the AGIO surface. With the design, it was found that the shell of CaP precipitate played a pivotal role not only in acting as a drug depot, but also in rendering the drug release rate with a highly controlled, pH-dependent manner. While the core–shell nanoparticles are well characterized in terms of nanostructural evolution, chemical structure, imaging modality and drug release behavior, these drug-loaded nano-objects also demonstrated high biocompatibility and efficient cellular internalization toward the HeLa cells, suggesting a promising multifunctional nanodevice for nanotherapeutic approaches.

2. Experimental

2.1. Materials

Absolute ethanol (99.5%), benzyl ether (99%), 1,2-hexadecanediol (97%), oleic acid (90%), oleylamine (>70%) and iron(III) acetylacetonate were purchased from Aldrich Chemical Co. Gelatin type A (Bloom 300), hexanol anhydride, calcium chloride, ammonium dihydrogen phosphate and sodium hydroxide were supplied by Sigma. Fluorescein isothiocyanate (FITC, Sigma) was used to label the nanoparticles for visualization under a fluorescence microscope. Doxorubicin hydrochloride was used as the model drug obtained from Sigma.

2.2. Synthesis of monodisperse iron oxide nanoparticles

Monodisperse iron oxide nanoparticles were synthesized by a method developed by Sun et al. [23]. Briefly, iron oxide nanoparticles were synthesized by mixing 2 mmol $Fe(acac)_3$ (iron III acetylacetonate), 10 mmol 1,2-dodecanediol, 6 mmol oleic acid, 6 mmol oleylamine and 20 ml benzyl ether under a constant flow of nitrogen. The mixture was stirred and preheated to reflux (200 °C) for 30 min, and then brought to 300 °C for another 1 h under nitrogen. The black–brown mixture was allowed to cool to room temperature, and then 50 ml ethanol was added for precipitation process. The products were collected by centrifugation at 6000 rpm for 10 min and then washed four times with an excess of pure ethanol. The product, iron oxide nanoparticles, was centrifuged to remove solvent, and redispersed in hexane.

2.3. Synthesis of AGIO nanoparticles

Amphiphilic gelatin was developed in the present authors' laboratory [22]. Briefly, 1.25 g of gelatin was taken up in 20 ml water, and the suspension was gently mixed with 2 ml of 0.1 M NaOH solution, and then the solution was stirred for 0.5 h at 70 °C. Subsequently, 4 ml of hexanol anhydride were added to 20 ml of gelatin hydrolyzate with stirring at 70 °C. After a reaction time of 5 h, the mixture was cooled to room temperature and adjusted with dilute sodium hydroxide to a pH value of 7.4. The resulting solutions were collected by dialysis tubing cellulose membrane after dialysis with ethanol solution (25% v/v) for 24 h. To obtain the powder form, the gel was then dried in the oven at 60 °C.

To prepare the AGIO nanoparticles, 5 mg of iron oxide nanoparticles were centrifuged at 6000 rpm for 10 min, and then redispersed in 0.5 ml chloroform to form a uniform organic phase. 100 mg of amphiphilic gelatin as a polymer binder was dissolved in 2 ml deionized (DI) water. After amphiphilic gelatin had been completely dissolved in the solution, the organic phase was added into the reaction solution. The mixture was emulsified for 1 min with an ultrasonicator at 50 W. During ultrasonication, the mixture was heated to evaporate the organic solvent. Afterwards, the mixture was stirred and heated again to 50 °C on a hot plate to ensure complete removal of the organic phase. The final products were washed three times with DI water, and then centrifuged at 12,000 rpm for the collection of the precipitates.

2.4. Synthesis of AGIO@CaP nanoparticles

Five milliliters of DI water was mixed with 60 μl of 0.1 M (NH_4)-H_2PO_4 and 100 μl of 0.1 M NaOH (pH 10). Then, 100 μl of 0.1 M $CaCl_2$ and 2 mg of AGIO nanoparticles prepared as described were added consecutively, while the suspension was stirred at 400 rpm under room temperature (typically 25 °C). The suspension was stirred for an additional 30 min before analysis and storage. The final product was collected via centrifugation at 12,000 rpm and decantation of the supernatant.

2.5. Characterization of nanoparticles

The morphology of AGIO nanoparticles and AGIO@CaP core–shell nanoparticles was examined using transmission electron microscopy (TEM; JEM-2100, Japan). Fourier transform infrared (FT-IR) spectra were obtained with attenuated total reflectance FT-IR (ATR-FTIR) spectroscopy, and the results were recorded on a spectrometer (Bomem DA8.3, Canada) which can be used to identify the crystallographic phase of CaP coated on AGIO nanoparticles. Meanwhile, energy dispersive X-ray (EDX) spectroscopy was used to calculate the Ca/P molar ratio of the AGIO@CaP nanoparticles. The magnetization of the AGIO, AGIO@CaP and AGIO@CaP-DOX nanoparticles was measured using a superconducting quantum interference device (SQUID; MPMS-XL7) at 298 K and ±10000 G applied magnetic field. Before carrying out the SQUID analysis, the AGIO, AGIO@CaP and AGIO@CaP-DOX nanoparticles were vacuum dried for 2 days at 60 °C.

MR in vitro assays were performed using a 7 Tesla Rodent MRI Scanner (BioSpec 70/30, Bruker Topspin, Ettlingen, Germany).T_1 relaxivity (r_1) and T_2 relaxivity (r_2) were determined by diluting AGIO, AGIO@CaP and AGIO@CaP-DOX nanoparticles with 0.5% agarose gel at Fe concentrations of 0.00, 0.06, 0.10, 0.25 and 0.47 mM. A quadrature-volume coil with an inner diameter of 112 mm was used for RF transmission and reception. Both T_1 and T_2 weighted images were obtained by the multi-slice multi-echo (RARE; TE = 10.5 ms, TR = 1300 ms, SLTH = 1 mm, acquisition matrix 384×192 field of view (FOV) = 5.0×2.5 cm^2, NEX = 10) and fast spin echo (Turbo RARE; TE = 33 ms, TR = 2500 ms, SLTH = 1 mm, acquisition matrix 384×192 FOV = 5.0×2.5 cm^2, NEX = 6) sequences, respectively.

2.6. Synthesis of AGIO@CaP-DOX nanoparticles

Five milliliters of DI water was mixed with 60 μl of 0.1 M (NH_4)-H_2PO_4 and 100 μl of 0.1 M NaOH (pH 10). To this solution were added 100 μl of 0.1 M $CaCl_2$, 2 mg of AGIO nanoparticles and 2 ml of the solution with 25 μg ml^{-1} of DOX, while the suspension was stirred at 400 rpm under room temperature (typically 25 °C). After reaction for 1 h, the suspension was washed three times with DI water and then centrifuged at 12,000 rpm to collect the products. Free DOX was removed by centrifugation at 12,000 rpm and

4 °C for 10 min. Drug concentration in the supernatant was analyzed using ultraviolet (UV) absorption at a wavelength of 490 nm, a strong absorption band of DOX, with reference to a calibration curve on a UV–Vis spectrometer (Agilent, 84531 UV–Visible spectrophotometer). The encapsulation efficiency (EE) was obtained using the following equation:

$$EE = (L_1 - L_2)/L_1 \times 100 \quad (1)$$

where L_1 is the total amount of DOX, and L_2 is the amount of DOX remaining in the supernatant.

2.7. Drug release of AGIO@CaP-DOX nanoparticles

Phosphate buffered saline (PBS) of pH 7.4 and acetic buffer solutions of pH 5, 5.5 and 6.5 were used as the drug release media to simulate normal blood/tissues and tumor environments. The AGIO@CaP-DOX nanoparticles were dispersed into 2 ml release media, and then the solutions were put into pretreated dialysis bags (M_w cutoff = 12,400 kDa). The dialysis bags were placed into brown bottles, and then 8 ml of release media was added. These bottles were shaken at a speed of 100 rpm at 37 °C under a light-sealed condition. At certain time intervals, the medium was withdrawn and replaced with an equal volume of fresh medium. The concentration of DOX released from the nanoparticles was estimated by measuring the absorbance at 490 nm.

2.8. Cell viability

A comparison of the in vitro cytotoxicity of AGIO and AGIO@CaP was performed on HeLa cells using an in vitro proliferation method and MTT. Briefly, 1×10^4 cells well^{-1} were plated in 96-well plates and exposed to the serial concentrations of AGIO and AGIO@CaP at 37 °C for 24 h. Subsequently, 20 ml of MTT solution (5 mg ml^{-1} in PBS, pH 7.4) was added, and the cells were incubated for an additional 4 h. Then the medium was replaced with 200 ml of DMSO, and the absorbance was monitored using a Sunrise absorbance microplate reader at the dual wavelengths of 595 nm. Cell viability was determined by comparison with untreated cells and calculated according to the following equation:

$$\text{Cell viability}(\%) = (A_{\text{sample}}/A_{\text{control}}) \times 100\%$$

2.9. Confocal laser scanning microscopy (CLSM) observation

HeLa cells were cultured with 1.5 ml of DMEM containing 10% FBS on 6-well plates at 5×10^4 cells well^{-1}. After incubation for 24 h, the medium was replaced with a fresh one, and the AGIO@CaP-FITC nanoparticles were applied to the well at a concentration of 20 μg ml^{-1}. After various times, the medium was discarded, and the cells were washed three times with PBS. Then the endosomes/lysosomes were stained with LysoTracker Red (Molecular Probes, Eugene, OR) for 2 h. The cells were fixed with 3% formaldehyde (in PBS) for 30 min and washed with PBS. Then 0.1% Triton X-100 was added in the wells for 15 min and washed with PBS. Subsequently, the nuclei of cells were stained with 4′,6-diamidino-2-phenylindole (DAPI, 1 μg ml^{-1}) for 1 h. Finally, stained samples were mounted on clean glass slides using mounting solution and observed by confocal laser scanning microscopy (Axiovert 100 M). In addition, the AGIO@CaP-DOX nanoparticles were added to the well at a concentration of 20 μg ml^{-1}. After various periods, the medium was discarded, and the cells were washed three times with PBS. Then the endosomes/lysosomes were stained with LysoTracker Green for 2 h. The cells were fixed with 3% formaldehyde for 30 min and washed with PBS. Then 0.1% Triton X-100 was added in the well for 15 min and washed with PBS. Subsequently, the nuclei of cells were stained with DAPI (1 μg ml^{-1}) for 1 h. The cells were rinsed three times with PBS and mounted on clean glass slides for observation by CLSM (Axiovert 100 M).

3. Results and discussion

3.1. Preparation of AGIO@CaP nanoparticles

The synthetic scheme of AGIO@CaP nanoparticles is illustrated in Fig. 1, from which the core phase is virtually a mixture of oleic acid-modified magnetic nanocrystallites and the amphiphilic gelatin. The interaction between the adsorbed oleic acids and hydrophobic segments of the amphiphilic gelatin should provide sufficient affinity to aggregate the magnetic nanocrystallites within the gelatin network. Upon self-assembly, the amphiphilic gelatin induced structural aggregation of the iron oxide nanocrystallites to form the aggregated core, which is potentially equipped with an MR imaging modality over the resulting nanoparticles. Taking advantage of the negatively charged carboxyl groups along the surface of amphiphilic gelatin, the subsequent electrostatic interactions of positively charged Ca^{2+} ions toward carboxyl group permits the deposition of CaP mineral on the surface of the AGIO core [24,25]. With increasing deposition time, more CaP precipitates formed on the core surface, resulting in a CaP shell with appreciable thickness, giving a final spherical core–shell nanoparticle. Fig. 2a shows the AGIO nanoparticles with an average diameter of 80 nm, while in Fig. 2b, after CaP shell formation, the AGIO@CaP nanoparticles show an average size of ~120 nm and a shell thickness of ~20 nm. The magnified and high-resolution TEM images of the AGIO@CaP nanoparticles in Fig. 2c and d, respectively, further demonstrate the amorphous structure of CaP shell [26], suggesting rapid CaP formation over a short period of exposure in the CaP precursor solution. The character of the amorphous CaP phase also rendered high responsiveness toward acidic dissolution [15,27]. In addition, either AGIO or AGIO@CaP nanoparticles displayed uniform particle size distribution and well-dispersed character in Table 1 as determined by dynamic light scattering (DLS). The surface charge of the AGIO@CaP is determined as −12.3 mV, presumably due to surface PO_4^{3-} ions of the CaP shell.

3.2. Characterization of AGIO and AGIO@CaP nanoparticles

The FT-IR spectrum of AGIO nanoparticles in Fig. 3a shows a strong absorption band of Fe–O bonds at 680 cm^{-1} [28], indicating the appearance of iron oxide nanoparticles. For the AGIO@CaP nanoparticles, absorption bands at 608 and 1043 cm^{-1} were attributed to the characteristic peaks of O–P–O bending and asymmetric stretching of PO_4^{3-} ions [29], which suggested the presence of an apatite-like phase. Elemental analyses were performed using the EDX technique, as shown in Fig. 3b, where a Ca/P molar ratio of ~1.5 was calculated over the detection region along the CaP shell of the AGIO@CaP nanoparticle. The Ca/P molar ratio obtained suggested the shell being a mineral of amorphous calcium phosphate (ACP) [15]. Accordingly, such an ACP mineral should be more susceptible to dissolving in acidic environments. In other words, this amorphous CaP shell imparted high pH responsiveness to the AGIO@CaP nanoparticles. Table 1 also shows the content of the inorganic and organic components in AGIO and AGIO@CaP nanoparticles. The content of iron oxides, CaP precipitates and amphiphilic gelatin in AGIO@CaP nanoparticles calculated by thermogravimetric analysis was ~43.3, 31.4 and 25.3 wt.%, respectively (Supplementary Fig. S1). This demonstrated that CaP precipitates would affect the relative content of iron oxide in AGIO@CaP nanoparticles.

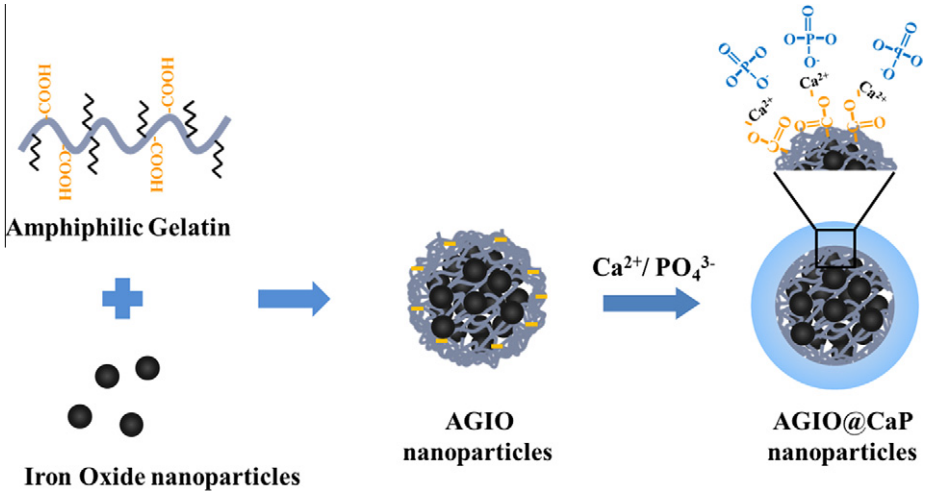

Fig. 1. The synthetic scheme of AGIO nanoparticles with CaP coating.

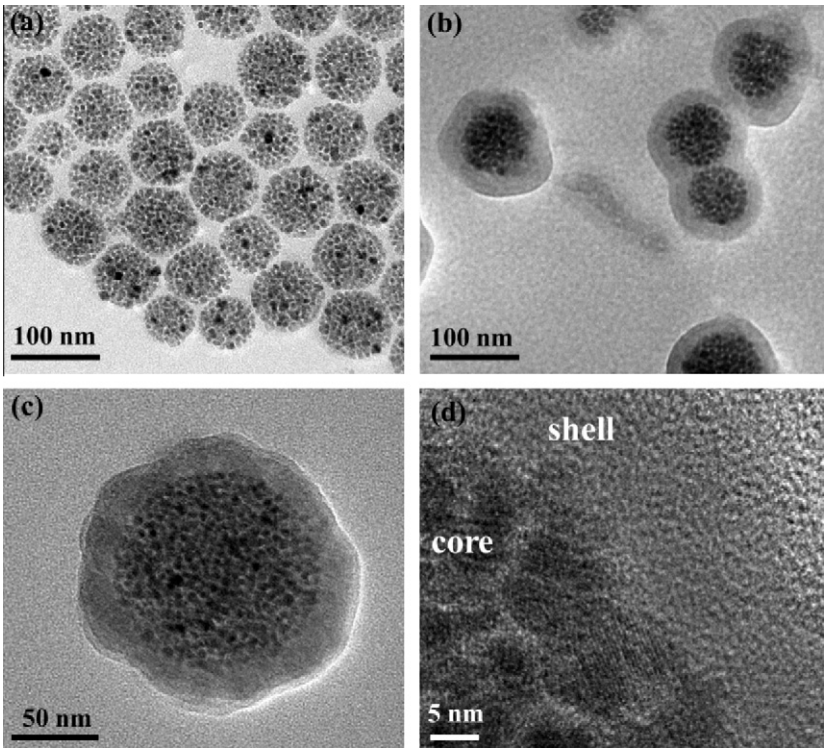

Fig. 2. TEM image of (a) AGIO nanoparticles and (b) AGIO@CaP nanoparticles. (c) Magnified and (d) High-resolution TEM image of AGIO@CaP nanoparticles.

Table 1
Characterization of AGIO and AGIO@CaP nanoparticles.

	Inorganic (wt.%)	Organic (wt.%)	Size[a] (nm)	Zeta[b] (mV)	Emu/g	Encapsulation efficiency (EE)
AGIO	63.1	36.9	80 ± 8	−23.7 ± 3.1	30.5	–
AGIO@CaP	74.7	25.3	120 ± 12	−12.3 ± 2.3	21.0	38%

[a] Size and size distribution determined by the DLS method with three trials.
[b] Zeta potential measured by a photon correlation spectrometer with three trials.

The magnetic properties of the AGIO, AGIO@CaP and AGIO@CaP-DOX nanoparticles were determined by SQUID at 298 K, with the magnetic field sweeping from −10000 to +10000 G. In Fig. 3c, the correlation of the magnetization curves with the magnetic field for the AGIO, AGIO@CaP and AGIO@CaP-DOX nanoparticles showed similar shape with negligible hysteresis. The saturation magnetization (M_s) values of the AGIO, AGIO@CaP and AGIO@CaP-DOX nanoparticles were 30.5, 21.0 and 19.3 emu g^{-1}. The presence

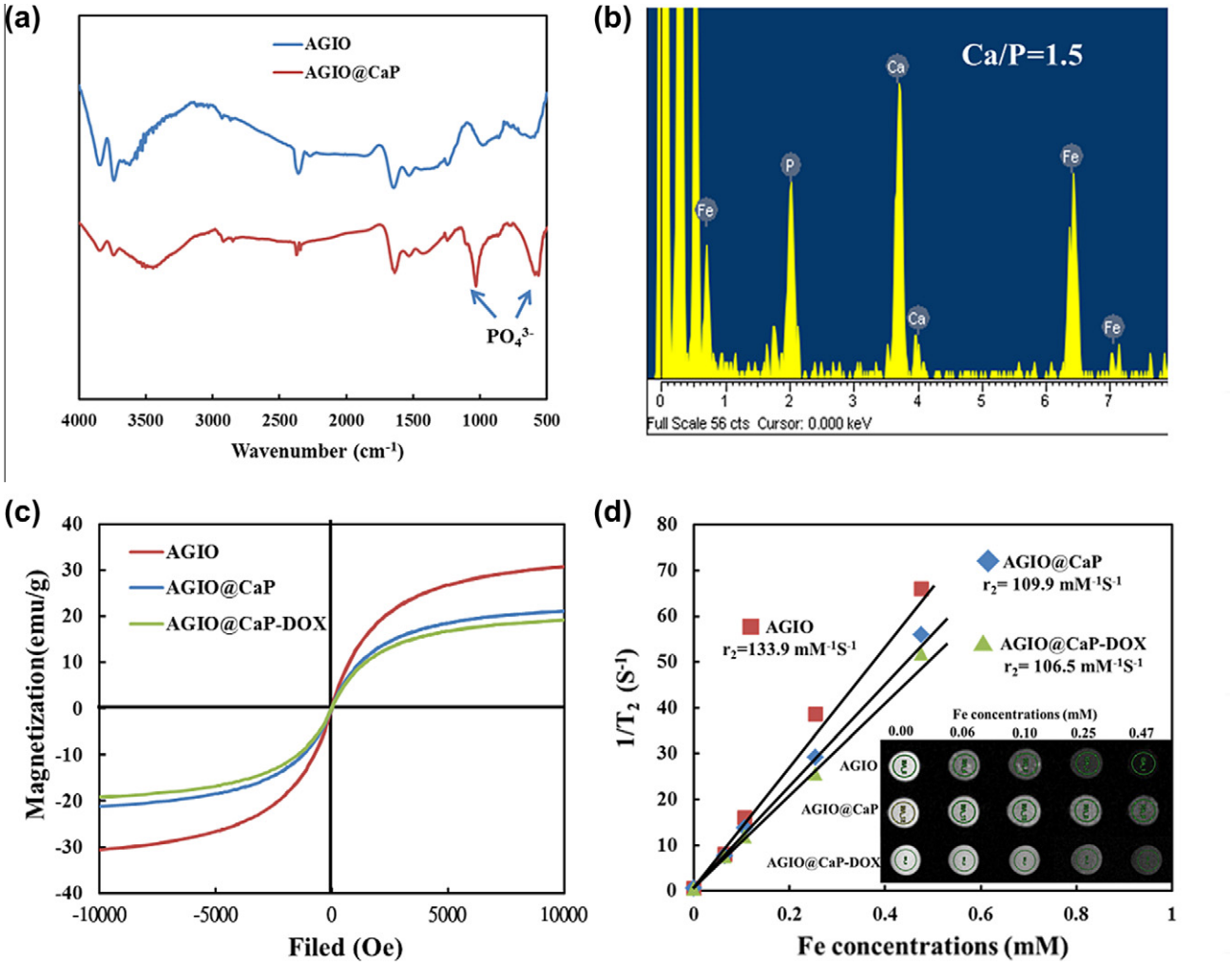

Fig. 3. (a) FT-IR spectra of AGIO and AGIO@CaP nanoparticles. (b) EDX spectroscopy analysis of the AGIO@CaP nanoparticles, showing Ca/P molar ratio = 1.5. (c) Magnetization (M) loop from the SQUID analysis of AGIO, AGIO@CaP and AGIO@CaP-DOX nanoparticles. (d) T_2-relaxivity plots of aqueous suspension of AGIO, AGIO@CaP and AGIO@CaP-DOX nanoparticles with the inset to show the signal strength of bare AGIO, AGIO@CaP and AGIO@CaP-DOX nanoparticles at various Fe dilutions.

of CaP could dilute the concentration of magnetic nanoparticles, resulting in a lower M_s of the AGIO@CaP nanoparticles than that of the AGIO nanoparticles [30]. The absence of a hysteresis loop with reversal of the magnetic field indicated that no magnetic energy was lost, which is relatively consistent with that observed from typical superparamagnetic behavior. The superparamagnetic characteristics of the AGIO,AGIO@CaP and AGIO@CaP-DOX nanoparticles could be used as a T_2 contrast agent in MR imaging. The T_2 relaxation times of protons from the dispersion containing AGIO, AGIO@CaP and AGIO@CaP-DOX nanoparticles are shown in the inset of Fig. 3d, where the MR signal decreases with increasing content of nanoparticles. This observation clearly confirmed that the nanoparticles prepared in this work are able to enhance the T_2 proton relaxation process. The relaxivity values (r_2) of the AGIO, AGIO@CaP and AGIO@CaP-DOX nanoparticles were further evaluated as 133.9, 109.9 and 106.5 $mM^{-1}\ s^{-1}$, respectively, as given in Fig. 3d. Although the r_2 of the AGIO nanoparticles exhibited a higher value than that of the AGIO@CaP nanoparticles, the r_2 level originating from the AGIO@CaP nanoparticles could still provide reasonably high magnetization resolution towards MR imaging. Therefore, as a designated multifunctional carrier, the resulting AGIO@CaP nanoparticles should be a potential T_2-type MR contrast enhancement agent for imaging and diagnostic applications.

3.3. Formation of AGIO@CaP nanoparticles and drug release

The schematic drawing in Fig. 4a shows the synthesis process for the formation of CaP and CaP-DOX shell on an AGIO core. For the growth mechanism of DOX-free CaP shell on the AGIO core in the early stage (i.e., reaction time 30 s), free Ca^{2+} cations adsorbed around the core by electrostatic interactions of carboxyl group, which caused the nucleation of CaP to form a thinner shell on the core (Fig. 4b). As the reaction proceeded, a thick shell was formed, as illustrated in Fig. 2c. In contrast, when the CaP precursor and DOX were co-deposited on the surface of the AGIO core at the same time, the CaP-DOX shell was grown because both positively charged DOX molecules and Ca^{2+} simultaneously deposited and reacted with the negatively charged carboxyl groups on the core. The formation mechanism of CaP-DOX shell is illustrated in Fig. 4a. In the early stage (i.e., 30 s), the CaP nuclei were rapidly nucleated from the adsorbed cations, as evidenced in Fig. 4c. Then CaP nuclei continued growing with increasing deposition time, and formed a thick shell in the late stage as shown in Fig. 4d. The size and shell thickness of AGIO@CaP-DOX nanoparticles were estimated to be ~160 and 40 nm, respectively. In comparison with the DOX-free CaP shell in Fig. 2c, the co-deposition with DOX appeared to cause more roughened surface, and the volume of CaP-DOX shell increased ~2.3 times. In the meantime, the Ca/P molar ratio was reduced to ~1.33, which is less than that (i.e., 1.50) of DOX-free CaP.

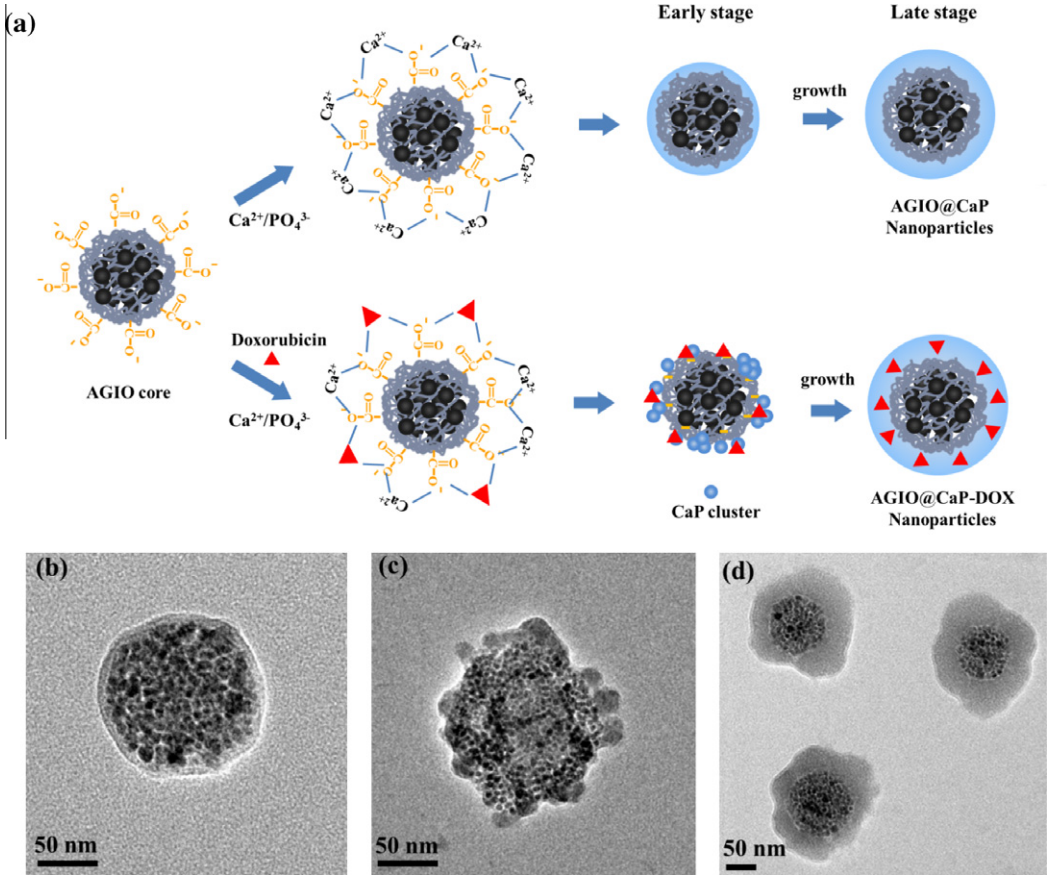

Fig. 4. (a) Schematic drawing illustrating the formation of CaP and CaP-DOX shell on AGIO core. TEM image of (b) AGIO@CaP and (c) AGIO@CaP-DOX nanoparticles in earlier reaction stage of 30 s. (d) TEM image of AGIO@CaP-DOX nanoparticles after reaction for 1 h.

In this case, the enhanced volumes and reduced Ca/P molar ratio are evidenced to suggest the presence of DOX molecules on the co-deposition of CaP-DOX shell.

The EE of AGIO@CaP-DOX was found to be 38%. For comparison, a two-stage deposition was also performed. DOX molecules with positive charge were adsorbed on the core by electrostatic interaction. Subsequently, the excess DOX was removed, and then the CaP precursors were added to grow the shell on the AGIO core. However, it was found that the *EE* of drug was ~10%, much lower than that of AGIO@CaP-DOX by a co-deposition process. Considering the water-soluble property of the anti-cancer drug DOX, a co-deposition of DOX and CaP was carried out onto the AGIO core. Such a simultaneous formation of CaP-DOX nanostructure ensures a number of advantages (such as avoiding early phase leakage during multi-stage process of drug encapsulation, controllable drug payload and ease of drug loading) over existing alternatives, which are frequently conducted in a two-stage process: drug loading either in core phase or on core surface, followed by coating with a protective shell of CaP.

Accordingly, CaP-DOX shell with a Ca/P ratio of ~1.33 can be referred to as octacalcium phosphate, which is considered a precursor for the apatitephase, and should be much less chemically stable compared withDOX-free CaP coating with a ratio of 1.50. Further examination of the CaP-DOX shell revealed a similar amorphous structure that evolved along the AGIO core surface in the same way as that of DOX-free CaP coating. In combination with its poor chemical stability (because of large deviation from stoichiometric chemistry of apatite or tricalcium phosphate) and amorphous nature, the designated CaP-DOX shell should be more pH sensitive and less structurally stable than CaP with higher Ca/P ratios. On this basis, an enhanced pH responsive behavior can be expected, which allows a design of highly pH-sensitive drug elution to be technically feasible.

Fig. 5a shows the drug release of the AGIO@CaP-DOX nanoparticles in solutions with different pH values. The DOX release exhibited a relatively slow profile at pH 7.4, i.e., <20% for a period of 24 h, suggesting the CaP shell was acting as a structurally stable phase at physiological pH and effective barrier for DOX diffusion. A rapid release of the DOX molecules from the surface or near-surface regions was clearly observed from the release profile at early phase duration. However, the enhanced release kinetics were detected for the acidic solution with pH 5.0, which reached 100% of DOX elution after immersion for a time of 10 h. Such a remarkable variation in release profile at different solution pH substantiates the pH responsiveness of the CaP shell. In order to model the kinetics of the drug release profile from the currently designed carriers, various mathematical equations were applied. The kinetics of DOX release from AGIO@CaP-DOX nanoparticles were evaluated according to zero-order kinetics, first-order kinetics and Higuchi models. The drug release kinetics was obtained by fitting the equations with the measured experimental data (Supplementary Fig. S2), and the resulting correlation indicated that DOX release from AGIO@CaP-DOX nanoparticles can be best described through Higuchi models, with a correlation coefficient as high as 0.99, compared with others [31]. The Higuchi model states that the drug release of carriers is proportional to the square root of time, which could be expressed by the following equation:

$$Q = K_H t^{1/2}$$

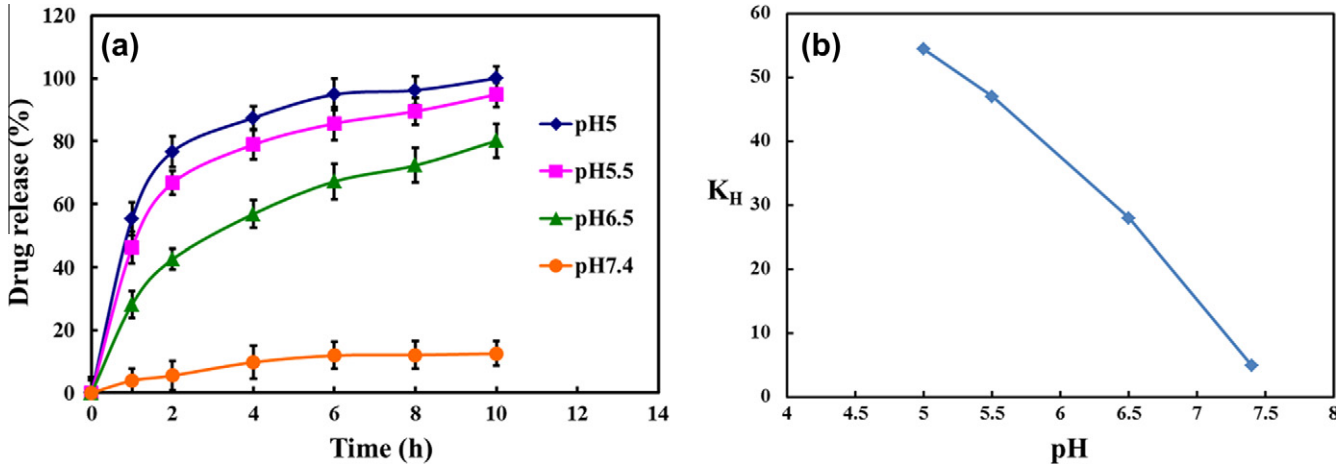

Fig. 5. (a) Drug release profiles from AGIO@CaP-DOX under different pH solutions, and (b) rate constant K_H changing with the pH values.

Q is the amount of drug released in time t, and K_H is the Higuchi rate constant. According to the Higuchi model, it is reasonable to believe that the DOX release profile from these nanoparticles may be controlled by diffusion [32]. The rate constant from the Higuchi model K_H is plotted as a function of pH value, as shown in Fig. 5b, where a remarkable enhancement by more than 10 times of diffusion rate of drug release from AGIO@CaP-DOX nanoparticles was determined from pH = 5.0 to pH = 7.4. This implies that the embedded DOX molecules were released out of the CaP matrix, because the CaP shell was suffering from acidic dissolution, which in turn affected the kinetics of drug release. This finding indicates that a highly pH-sensitive AGIO@CaP-DOX nanoparticle is successfully constructed via a co-deposition process of CaP shell [27,33].

Under acidic dissolution, the CaP-DOX shell should be subjected to structural disruption, as evidenced in Fig. 6, which demonstrates the process of structural collapse of AGIO@CaP-DOX nanoparticles under pH 5.5 and pH 6.5 at various times. Under pH 5.5 for 2 h, Fig. 6a shows that the shell of AGIO@CaP-DOX nanoparticles became thinner, and the thickness was reduced to ~8 nm by acidic etching. After 4 h, Fig.6b displays a disintegrated shell structure. Subsequently, the shell completely disappeared after 8 h acidic etching, as evidenced in Fig. 6c. In contrast, Fig. 6d shows that the shell of AGIO@CaP-DOX nanoparticles was still maintained with a thickness of ~19 nm under pH 6.5 after 2 h, indicating that the CaP was less dissolved in a high pH solution, but continuously removed to form a rough surface and extensively fractured structure in 4 h and 8 h, as shown in Fig.6e and f, respectively. In comparison with the DOX release in Fig. 5a, the rapid dissolution of CaP under pH 5.5 corresponds to the rapid DOX-released behavior at lower pH solution.

3.4. Cell uptake and intracellular trafficking

The cytocompatibility of the nanoparticles was further evaluated using HeLa cells. Fig. 7a shows the cell viability after incubation for 24 h with the AGIO@CaP nanoparticles at various concentrations from 0 to 1000 μg ml^{-1}. The results demonstrated

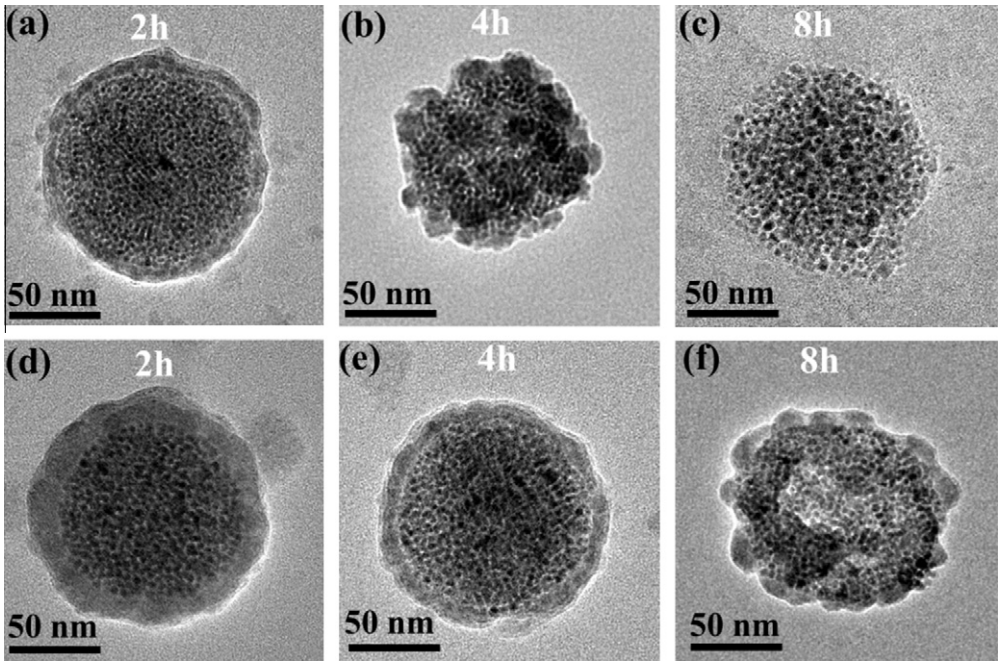

Fig. 6. Morphology evolution of AGIO@CaP-DOX nanoparticles for different times under (a–c) pH 5 and (d–f) pH 6.5.

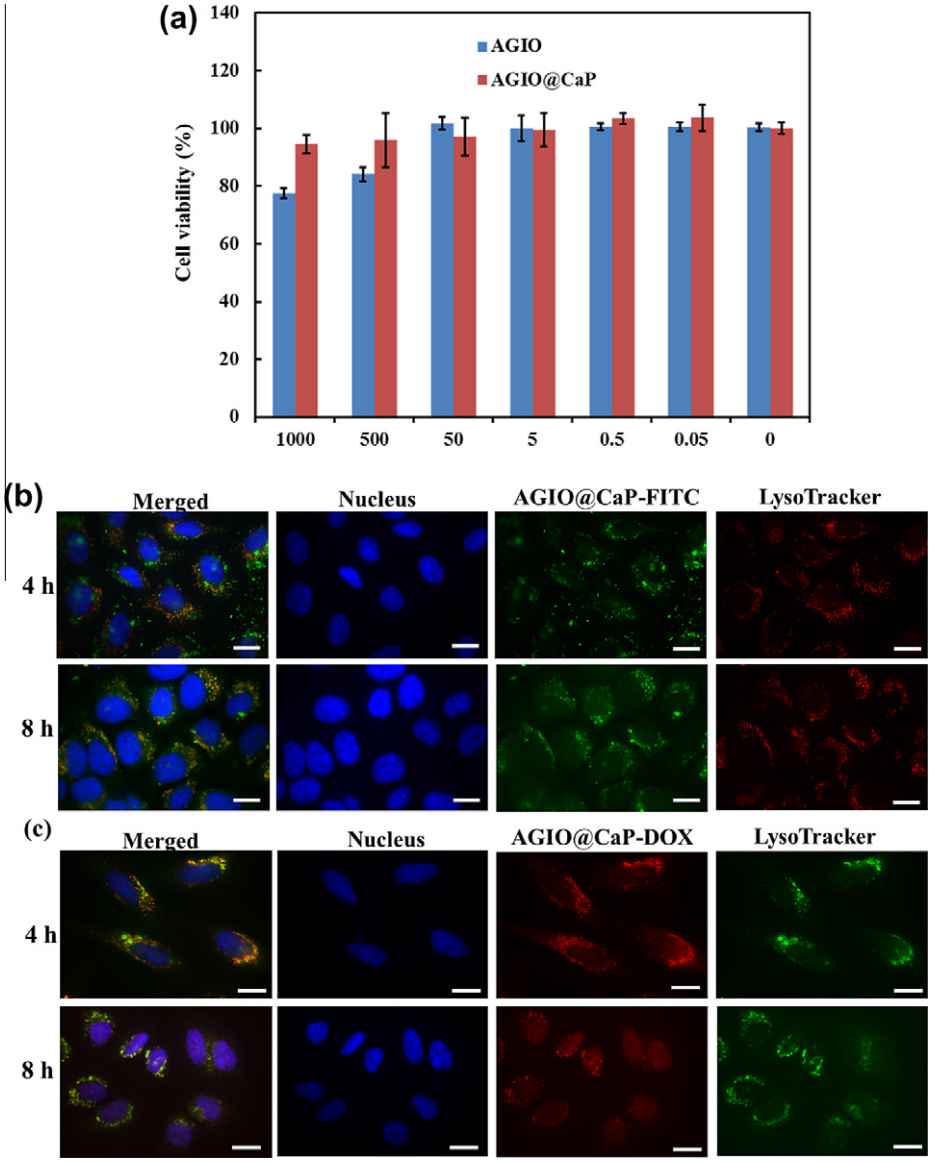

Fig. 7. (a) Cell viability of HeLa cells after incubation for 24 h with increasing amounts of AGIO and AGIO@CaP nanoparticles. (b) CLSM images of HeLa cells treated with LysoTracker after AGIO@CaP/FITC nanoparticles had been incubated for 4 and 8 h (scale bar: 20 μm). (c) CLSM images of HeLa cells treated with AGIO@CaP-DOX nanoparticles incubated for 4 and 8 h (scale bar: 20 μm).

that HeLa cells remained highly viable over a wide range of nanoparticle concentrations for those with CaPshell.In other words, the AGIO@CaP nanoparticles exhibited excellent biocompatibility and relatively low cytotoxicity compared with the AGIO nanoparticles. Such a comparison, although relatively preliminary, still reflected the highly biocompatible nature of the CaP mineral, to which an improved cytocompatibility, compared with the AGIO "bare" nanoparticles, can be achieved. The chemical similarity to nature bone minerals, e.g., apatite-like, imparts the synthetic ACP with a greater biological affinity toward hard tissues as well as soft tissues, as confirmed by the current cytocompatible evaluation. This is more interesting after a follow-up examination over its intracellular behavior. To address the issue, the AGIO@CaP nanoparticles with FITC were further exploited in the process of cellular uptake. Here, the intracellular trafficking of the AGIO@CaP-FITC nanoparticles by confocal laser scanning microscopy was examined at 4 and 8 h incubation with HeLa cells. Fig. 7b shows that the nanoparticles, endosomes/lysosomes and nuclei were shown in green, red and blue. The yellow pixels resulting from the merge of red and green pixels indicated the co-localization of AGIO@CaP-FITC nanoparticles with endosome/lysosome [34]. In these images, the nanoparticles containing FITC presented green spots, indicating the presence of AGIO@CaP-FITC in the HeLa cells, and the endosomes/lysosomes tracked by LysoTracker corresponded to red spots. The images of HeLa cells treated with the nanoparticles displayed perinuclear yellow spots, indicating that the nanoparticles allowed significant cellular uptake with endosomal/lysosomal capture. The images of HeLa cells treated with the AGIO@CaP/FITC nanoparticles displayed green and yellow spots after incubation for 4 h, indicating that the cellular uptake of the nanoparticles was not entirely complete. However, after incubation for 8 h, the yellow spots obviously increased to as many as the green spots, suggesting that more AGIO@CaP-FITC nanoparticles were internalized via endosomal mechanisms. Fig. 7c also suggests that the AGIO@CaP-DOX nanoparticles (Supplementary Fig. S3) were largely internalized by the HeLa cells. With increasing incubation time of the AGIO@CaP-DOX nanoparticles, DOX not only spread out in the lysosomes, but also accumulated in the nuclei. The red fluorescence intensity

was found in nuclei, which indicated that nanoparticles taken into the cells could dissolve at low pH. Subsequently, the dissolved calcium and phosphate ions increased the osmotic pressure and caused endosomal swelling. Finally, after dissolution of the CaP-DOX shell, DOX escaped from endosome and was delivered efficiently into the nucleus. The images with strong fluorescence intensity further supported that the AGIO@CaP-DOX nanoparticles were effectively internalized by the HeLa cells.

4. Conclusion

The amphiphilic gelatin assembled iron oxide (AGIO@CaP) nanoparticles were coated with a thinner shell (~20 nm) of CaP to form AGIO@CaP core–shell nanoparticles. Through a co-deposition forming technique, DOX-containing CaP shell was successfully achieved, which not only acts as an efficient drug reservoir, but also renders the resulting AGIO@CaP-DOX nanoparticles into highly pH-responsive drug release system. In addition, the AGIO@CaP-DOX nanoparticles demonstrated excellent cytocompatibility, efficient MR contrast and efficient cellular internalization toward HeLa cells. These biomedical features suggest the AGIO@CaP-DOX nanoparticles developed in this study area promising multifunctional nanodevice for anti-cancer applications.

Acknowledgments

This work is financially supported by the National Science Council of the Republic of China, Taiwan under Contract of NSC 100-2320-B-009-006-MY2 and NSC99-2221-E-009-070-MY3. This work is also supported by the "Aim for the Top University" program of the National Chiao Tung University and Ministry of Education, Taiwan, ROC.

Appendix A. Figures with essential colour discrimination

Certain figures in this article, particularly Figs. 1,3–5,7 are difficult to interpret in black and white. The full colour images can be found in the on-line version, at http://dx.doi.org/10.1016/j.actbio.2012.09.023.

Appendix B. Supplementary data

Supplementary data associated with this article can be found, in the online version, at http://dx.doi.org/10.1016/j.actbio.2012.09.023.

References

[1] Lee ES, Gao ZG, Bae YH. Recent progress in tumor pH targeting nanotechnology. J Control Release 2008;132:164–70.
[2] Yang Q, Wang SH, Fan PW, Wang LF, Di Y, Lin KF, et al. PH-responsive carrier system based on carboxylic acid modified mesoporous silica and polyelectrolyte for drug delivery. Chem Mater 2005;17:5999–6003.
[3] Su J, Chen F, Cryns VL, Messersmith PB. Catechol polymers for pH-responsive, targeted drug delivery to cancer cells. J Am Chem Soc 2011;133:11850–3.
[4] Meng HA, Xue M, Xia TA, Zhao YL, Tamanoi F, Stoddart JF, et al. Autonomous in vitro anticancer drug release from mesoporous silica nanoparticles by pH-sensitive nanovalves. J Am Chem Soc 2010;132:12690–7.
[5] Kang XJ, Cheng ZY, Yang DM, Ma PA, Shang MM, Peng C, et al. Design and synthesis of multifunctional drug carriers based on luminescent rattle-type mesoporous silica microspheres with a thermosensitive hydrogel as a controlled switch. Adv Funct Mater 2012;22:1470–81.
[6] Po-Jung C, Shang-Hsiu H, Chi-Sheng H, You-Yin C, Dean-Mo L, San-Yuan C. Multifunctional magnetically removable nanogated lids of Fe_3O_4-capped mesoporous silica nanoparticles for intracellular controlled release and MR imaging. J Mater Chem 2011;21:2535–25432543.
[7] Zhou T, Wu BY, Xing D. Bio-modified Fe_3O_4 core/Au shell nanoparticles for targeting and multimodal imaging of cancer cells. J Mater Chem 2012;22:470–7.
[8] Zhou LJ, Liang D, He XL, Li JH, Tan H, Li JS, et al. The degradation and biocompatibility of pH-sensitive biodegradable polyurethanes for intracellular multifunctional antitumor drug delivery. Biomaterials 2012;33:2734–45.
[9] Oishi M, Nakamura T, Jinji Y, Matsuishi K, Nagasaki Y. Multi-stimuli-triggered release of charged dye from smart PEGylated nanogels containing gold nanoparticles to regulate fluorescence signals. J Mater Chem 2009;19:5909–12.
[10] Qianjun H, Yu G, Lingxia Z, Zhiwen Z, Fang G, Xiufeng J, et al. A pH-responsive mesoporous silica nanoparticles-based multi-drug delivery system for overcoming multi-drug resistance. Biomaterials 2011;32:7711–77207720.
[11] Sousa A, Souza KC, Sousa EMB. Mesoporous silica/apatite nanocomposite: special synthesis route to control local drug delivery. Acta Biomater 2008;4:671–9.
[12] Lingzhou Z, Liangsheng H, Kaifu H, Yumei Z, Zhifen W, Chu PK. Mechanism of cell repellence on quasi-aligned nanowire arrays on Ti alloy. Biomaterials 2010;31:8341–83498349.
[13] Dorozhkin SV. Nanosized and nanocrystalline calcium orthophosphates. Acta Biomater 2010;6:715–34.
[14] Motskin M, Wright DM, Muller K, Kyle N, Gard TG, Porter AE, et al. Hydroxyapatite nano and microparticles: correlation of particle properties with cytotoxicity and biostability. Biomaterials 2009;30:3307–17.
[15] Dorozhkin SV, Epple M. Biological and medical significance of calcium phosphates. Angew Chem Int Ed 2002;41:3130–46.
[16] Sokolova V, Knuschke T, Buer J, Westendorf AM, Epple M. Quantitative determination of the composition of multi-shell calcium phosphate–oligonucleotide nanoparticles and their application for the activation of dendritic cells. Acta Biomater 2011;7:4029–36.
[17] Li J, Chen YC, Tseng YC, Mozumdar S, Huang L. Biodegradable calcium phosphate nanoparticle with lipid coating for systemic siRNA delivery. J Control Release 2010;142:416–21.
[18] Bose S, Tarafder S. Calcium phosphate ceramic systems in growth factor and drug delivery for bone tissue engineering: a review. Acta Biomater 2012;8:1401–21.
[19] Lee HJ, Kim SE, Kwon IK, Park C, Kim C, Yang J, et al. Spatially mineralized self-assembled polymeric nanocarriers with enhanced robustness and controlled drug-releasing property. Chem Commun 2010;46:377–9.
[20] Yeo CH, Zein SHS, Ahmad AL, McPhail DS. Comparison of DOPA and DPPA liposome templates for the synthesis of calcium phosphate nanoshells. Ceram Int 2012;38:561–70.
[21] Yurong C, Haihua P, Xurong X, Qinghong H, Ling L, Ruikang T. Ultrasonic controlled morphology transformation of hollow calcium phosphate nanospheres: a smart and biocompatible drug release system. Chem Mater 2007;19:129–131131.
[22] Li WM, Liu DM, Chen SY. Amphiphilically-modified gelatin nanoparticles: self-assembly behavior, controlled biodegradability, and rapid cellular uptake for intracellular drug delivery. J Mater Chem 2011;21:12381–8.
[23] Sun SH, Zeng H, Robinson DB, Raoux S, Rice PM, Wang SX, et al. Monodisperse MFe_2O_4 (M = Fe, Co, Mn) nanoparticles. J Am Chem Soc 2004;126:273–9.
[24] Huang C, Zhou YB, Tang ZM, Guo X, Qian ZY, Zhou SB. Synthesis of multifunctional Fe_3O_4 core/hydroxyapatite shell nanocomposites by biomineralization. Dalton Trans 2011;40:5026–31.
[25] Schmidt HT, Gray BL, Wingert PA, Ostafin AE. Assembly of aqueous-cored calcium phosphate nanoparticles for drug delivery. Chem Mater 2004;16:4942–7.
[26] Zhang HQ, Darvell BW. Morphology and structural characteristics of hydroxyapatite whiskers: effect of the initial Ca concentration, Ca/P ratio and pH. Acta Biomater 2011;7:2960–8.
[27] Han SY, Han HS, Lee SC, Kang YM, Kim IS, Park JH. Mineralized hyaluronic acid nanoparticles as a robust drug carrier. J Mater Chem 2011;21:7996–8001.
[28] Park JW, Bae KH, Kim C, Park TG. Clustered magnetite nanocrystals cross-linked with PEI for efficient siRNA delivery. Biomacromolecules 2011;12:457–65.
[29] Zhang XJ, Lin DY, Yan XH, Wang XX. Evolution of the magnesium incorporated amorphous calcium phosphate to nano-crystallized hydroxyapatite in alkaline solution. J Cryst Growth 2011;336:60–6.
[30] Shang-Hsiu H, Dean-Mo L, Wei-Lin T, Chen-Fu L, San-Yuan C. Surfactant-free, self-assembled PVA-iron oxide/silica core–shell nanocarriers for highly sensitive, magnetically controlled drug release and ultrahigh cancer cell uptake efficiency. Adv Funct Mater 2008;18:2946–29552955.
[31] Yan SF, Zhu J, Wang ZC, Yin JB, Zheng YZ, Chen XS. Layer-by-layer assembly of poly(L-glutamic acid)/chitosan microcapsules for high loading and sustained release of 5-fluorouracil. Eur J Pharm Biopharm 2011;78:336–45.
[32] Khoee S, Rahmatolahzadeh R. Synthesis and characterization of pH-responsive and folated nanoparticles based on self-assembled brush-like PLGA/PEG/AEMA copolymer with targeted cancer therapy properties: a comprehensive kinetic study. Eur J Med Chem 2012;50:416–27.
[33] Banerjee SS, Roy M, Bose S. pH tunable fluorescent calcium phosphate nanocomposite for sensing and controlled drug delivery. Adv Eng Mater 2011;13:B7–B10.
[34] Pittella F, Zhang MZ, Lee Y, Kim HJ, Tockary T, Osada K, et al. Enhanced endosomal escape of siRNA-incorporating hybrid nanoparticles from calcium phosphate and PEG-block charge-conversional polymer for efficient gene knockdown with negligible cytotoxicity. Biomaterials 2011;32:3106–14.